Twist-controlled resonant tunnelling in graphene/boron nitride/graphene heterostructures

A. Mishchenko[1], J. S. Tu[2], Y. Cao[2], R. V. Gorbachev[2], J. R. Wallbank[3], M. T. Greenaway[4], V. E. Morozov[1], S. V. Morozov[5], M. J. Zhu[1], S. L. Wong[1], F. Withers[1], C. R. Woods[1], Y-J. Kim[2,6], K. Watanabe[7], T. Taniguchi[7], E. E. Vdovin[4,5], O. Makarovsky[4], T. M. Fromhold[4], V. I. Fal'ko[3], A. K. Geim[1,2], L. Eaves[1,4] and K. S. Novoselov[1]*

Recent developments in the technology of van der Waals heterostructures[1,2] made from two-dimensional atomic crystals[3,4] have already led to the observation of new physical phenomena, such as the metal–insulator transition[5] and Coulomb drag[6], and to the realization of functional devices, such as tunnel diodes[7,8], tunnel transistors[9,10] and photovoltaic sensors[11]. An unprecedented degree of control of the electronic properties is available not only by means of the selection of materials in the stack[12], but also through the additional fine-tuning achievable by adjusting the built-in strain and relative orientation of the component layers[13–17]. Here we demonstrate how careful alignment of the crystallographic orientation of two graphene electrodes separated by a layer of hexagonal boron nitride in a transistor device can achieve resonant tunnelling with conservation of electron energy, momentum and, potentially, chirality. We show how the resonance peak and negative differential conductance in the device characteristics induce a tunable radiofrequency oscillatory current that has potential for future high-frequency technology.

The growing catalogue of two-dimensional (2D) crystals allows us to construct increasingly complex van der Waals heterostructures[7–11,18,19]. The combination of a hexagonal boron nitride (hBN) barrier layer sandwiched between two graphene electrodes is particularly attractive[7,8,20] because of the exceptional crystalline quality and the small lattice mismatch of these two materials. For example, by utilizing a third (gate) electrode, recently it was proved possible to make a novel type of field-effect transistor in which tunnelling between the two graphene electrodes is controlled by the gate voltage[9,21]. In the prototype versions of these devices, the crystalline lattices of the component layers were not intentionally aligned[7,8,20], which meant that tunnelling between the two graphene electrodes required a defect-assisted momentum transfer, so the tunnelling was not strictly resonant.

Here we report a new series of tunnel transistors in which the crystal lattices of the two graphene layers are intentionally aligned to a high degree of precision (within 2°) during the fabrication procedure. Our measurements and theoretical modelling of the device characteristics reveal that the current flow is dominated by tunnel transitions in which both energy and in-plane momentum are conserved. The resonant conditions exist in a narrow range of bias

voltages, and result in a resonant peak in the current–voltage characteristics, which leads to a strong negative differential conductance (NDC). In the NDC region, our devices generate radiofrequency oscillations when connected to a simple inductor–
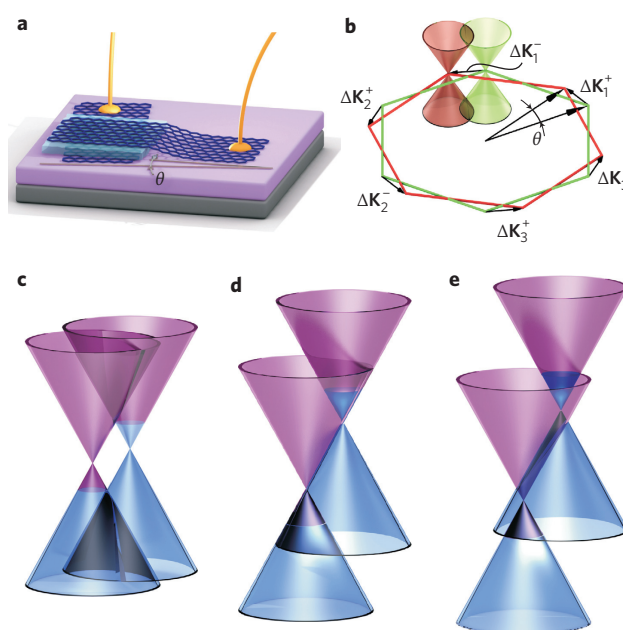
Figure 1 | Schematic representation of our device and its band structure. **a**, Device schematics with an exaggerated angle θ between two graphene layers (separated by a hBN tunnel barrier shown in light blue). The heterostructure is placed on a SiO$_x$/Si substrate (magenta/light grey), which serves as an electrostatic gate. Both graphene layers are independently contacted by Cr/Au metallization (yellow). **b**, A rotation by θ of the two graphene layers in real space corresponds to the momentum shift $\Delta\mathbf{K}_i^\pm$ between two Dirac points. **c-e**, Relative alignment between the top (left cones) and bottom (right cones) graphene Dirac points; the boundary between magenta (empty states) and blue (filled states) marks the Fermi level.

[1]School of Physics & Astronomy, University of Manchester, Oxford Road, Manchester M13 9PL, UK, [2]Centre for Mesoscience & Nanotechnology, University of Manchester, Manchester M13 9PL, UK, [3]Physics Department, Lancaster University, Lancaster University LA1 4YB, UK, [4]School of Physics and Astronomy, University of Nottingham, Nottingham NG7 2RD, UK, [5]Institute of Microelectronics Technology and High Purity Materials, Russian Academy of Sciences, Chernogolovka 142432, Russia, [6]Department of Chemistry, Seoul National University, Seoul 151-747, Korea, [7]National Institute for Materials Science, 1-1 Namiki, Tsukuba 305-0044, Japan. *e-mail: kostya@manchester.ac.uk

1
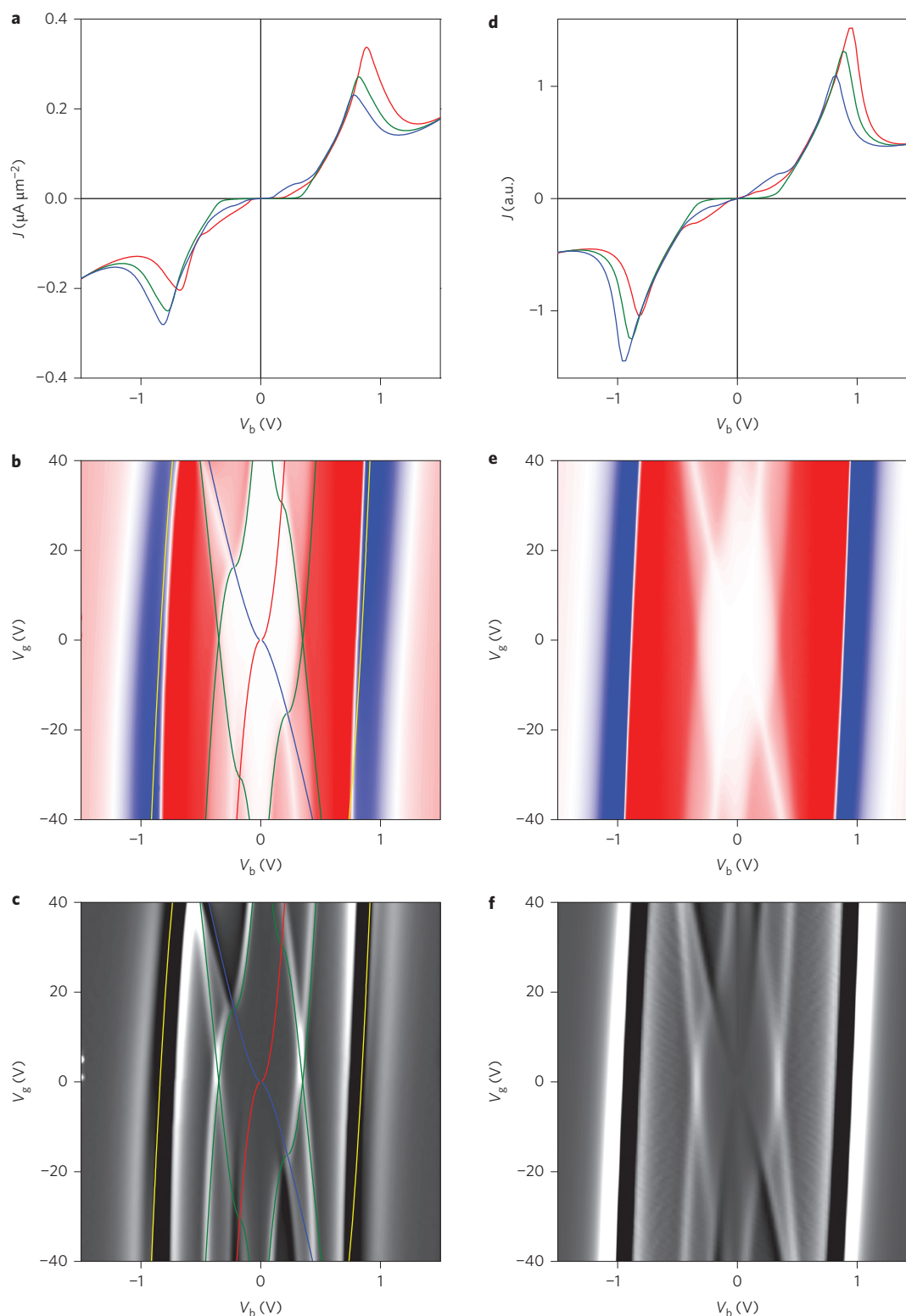
Figure 2 | The device characteristics at 2K. a–c, Experimental. **d–f**, Theoretical simulations. **a,d**, Current density–voltage curves at different V_g (red, green and blue lines for +40, 0 and –40 V, respectively). **b,e**, Conductance dI/dV plots as a function of V_b and V_g (colour scale is blue to white to red, –5 μS to 0 μS to 5 μS). **c,f**, |d^2I/dV^2| plots as a function of V_b and V_g (colour scales are arbitrary and matched for **c** and **f**). The solid lines in **b** and **c** are theoretical simulations and correspond to different resonant conditions. Red and blue lines correspond to events when the Fermi level in one of the graphene layers passes through the Dirac point. The green lines correspond to the event depicted in Fig. 1c, and the yellow lines to the event depicted in Fig. 1d. Device characteristics: active area ~8 μm^2, hBN barrier thickness 1.4 nm (four layers), $\theta \approx 1.8°$.

capacitor circuit. This proof-of-principle experiment points the way towards new applications for graphene-based resonant tunnelling devices in high-frequency electronics.

Figure 1a shows a schematic diagram of our transistor, and Fig. 2a shows the dependence of the current density, J, measured at 2 K as a function of the bias voltage, V_b, for three different
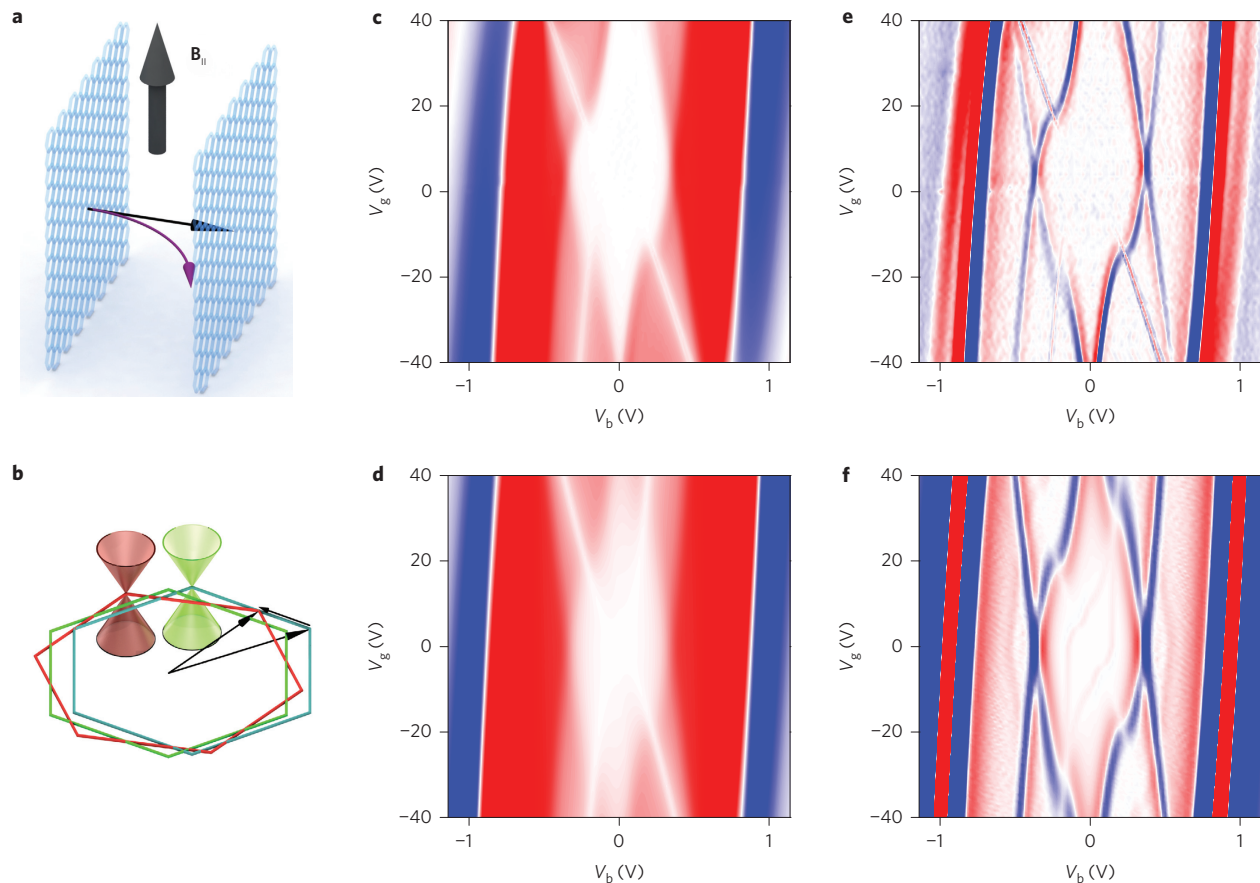
Figure 3 | Effect of an in-plane magnetic field on resonant tunnelling in the same device as in Fig. 2. a, Trajectories of the charged quasiparticles tunnelling from top (left) to bottom (right) graphene layers in zero (black arrow) and finite (purple arrows) magnetic fields (thick black arrow) caused by the Lorentz force. **b**, The resulting shift (green and blue hexagons) of the Fermi surface caused by an in-plane magnetic field, exaggerated for clarity. Here the red and green/blue hexagons represent corners of the Brillouin zones for the top and bottom graphene layers, respectively. **c–f**, Experimental data (**c,e**) and theoretical modelling (**d,f**). **c,d**, dI/dV maps measured with a 15 T in-plane magnetic field applied (colour scale is blue to white to red, –4 μS to 0 μS to 4 μS). **e,f**, Difference between the dI/dV maps with and without the in-plane B field (colour scale is blue to white to red, –0.4 μS to 0 μS to 0.4 μS).

values of the gate voltage, V_g. We observed a strong peak in $J(V_b)$, followed by a region of NDC, both of which persisted up to room temperature. We attribute this peak to resonant tunnelling of the carriers between the two graphene electrodes with momentum conservation. To display in more detail the key features of the device characteristics, Fig. 2b,c presents colour-scale contour maps of the dependence of the differential conductance (dI/dV_b) and d^2I/dV_b^2 on V_b and V_g, where I is the current. In Fig. 2b the regions of the NDC are shown as blue areas. Furthermore, weaker resonances can be seen as a transition from pink to red colours.

To explain the physics of the electron tunnelling in these devices, we used a theoretical model[22–25] that takes into account the unique band structure of graphene and the physics of the eigenstates of the massless Dirac fermions in the graphene layers on the device characteristics. The results of this model, shown in Fig. 2d–f, reproduce the measured device characteristics. Here we focus on the case of a small angular misalignment, θ, of the two graphene lattices (see Fig. 1a), which corresponds to a rotation of the two graphene Brillouin zones in momentum space (see Fig. 1b). In particular, the neutrality points at the six K points of the Brillouin zone, $\hbar \mathbf{K}_i^\pm$ (where $i = 1, 2$ and 3 identify equivalent corners, ± distinguishes between the K and K′ valleys and $\hbar$ is the reduced Plank constant) are displaced by the wavevectors $\Delta \mathbf{K}_i^\pm = \mathbf{l}_z \times \theta \mathbf{K}_i^\pm$.

The resulting intersections of the Dirac cones, which visualize the conditions for resonant tunnelling of electrons between two layers, are shown in Fig. 1c–e for characteristic regimes of bias

voltage. They display the energy shift of both Dirac cones and Fermi levels as the carrier concentrations in the two graphene layers change because of changes in the bias and gate voltages. Figure 1c and Fig. 1d illustrate how the conditions for resonant tunnelling can be satisfied. The case shown in Fig. 1d is of particular importance because the tunnel current is maximized when the momentum difference, ΔK, is compensated by changing electrostatically the energy difference of the two Dirac cones by an amount $\pm \hbar v_F \Delta K$ (valid for small θ; here v_F is the graphene Fermi velocity). In this case the conical dispersions in the two layers intersect along a straight line and a large fraction of the states along that line are occupied in one layer and empty in the other layer, which thus facilitates a large resonant tunnel current. Figure 1e demonstrates the case at a yet higher bias voltage between the top and bottom graphene layers, in which the in-plane momentum is conserved only for a small number of states (far away from the Fermi levels of the two graphene electrodes), and thus leads to a reduction in the current. We now consider the detailed features of the measured differential conductance map in Fig. 2c. The red and blue lines in Fig. 2c are theoretical simulations and correspond to the situation in which the Fermi levels of the top and bottom graphene layers pass through Dirac points. These lines are universal features for all graphene-to-graphene tunnelling systems regardless of their relative alignment, and can be obtained using a simple electrostatic model (see Supplementary Section 2). The density of states (DOS) of graphene close to the Dirac point varies linearly
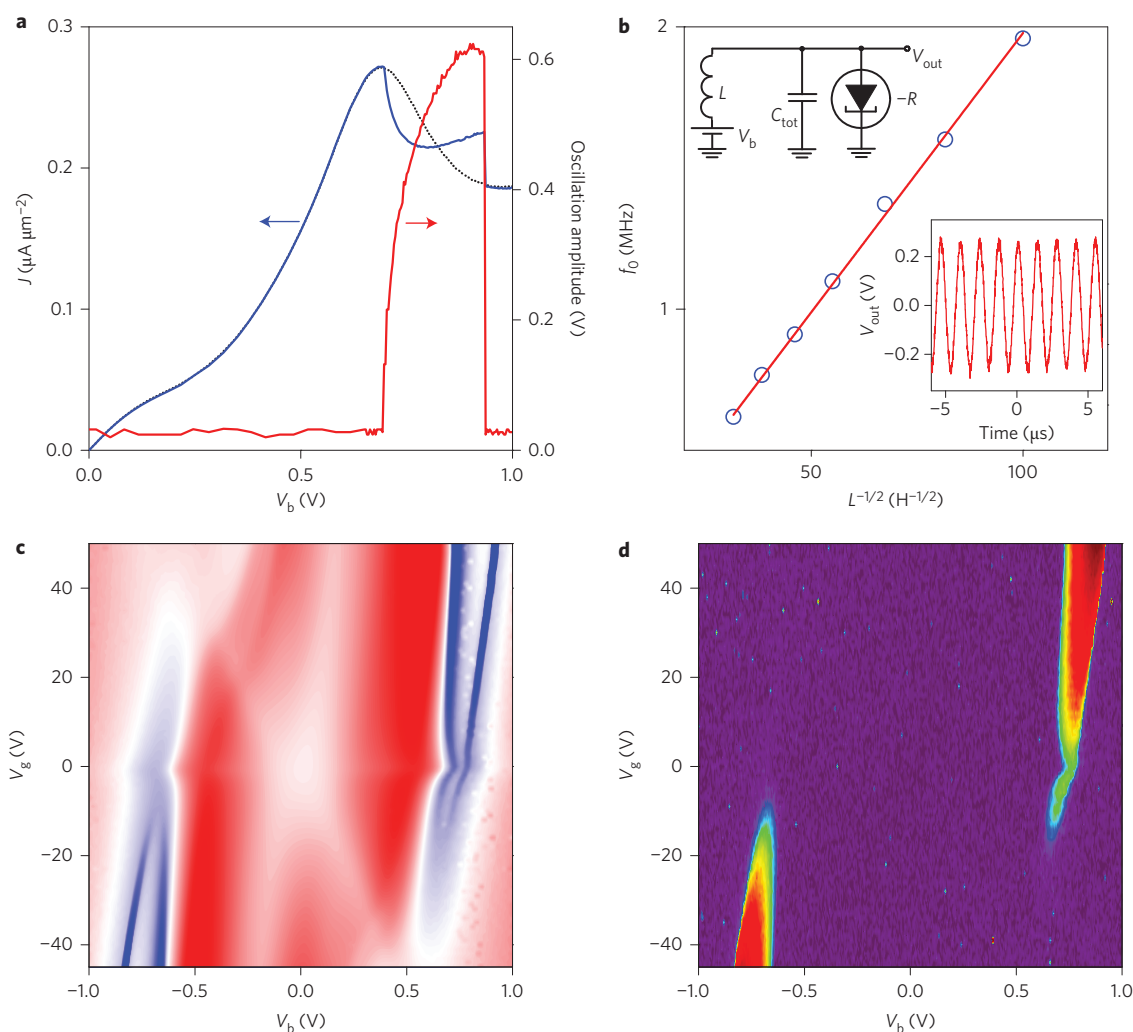
Figure 4 | Radiofrequency oscillator based on a resonant tunnelling transistor, _T_ = 300 K. a, $J(V_b)$ characteristics with (blue line, L = 1 mH) and without (dashed black line, L = 0 H) an external LC circuit (L, inductance; C_{tot}, total capacitance). The red curve shows the V_b dependence of the peak-to-peak amplitude of the oscillations. **b**, Resonant frequency of the oscillator (schematics shown in the top-left inset) versus the inductance of the LC circuit. For this device the total capacitance of the assembly was estimated from a simple circuit model (see top-left inset) to be 65 pF. The red line is a model fit to the data. Bottom-right inset shows V_{out} as a function of time for L = 1 mH. **c**, A dI/dV_b map measured with a 330 μH inductance (red to white to blue, –0.7 μS to 0 μS to 0.7 μS), **d**, Corresponding amplitude map (red to yellow to violet, 0.5 V to 0.26 V to 0.03 V). Device structure: active area ~120 μm², hBN spacer 1.4 nm (four layers), $\theta \approx 0.9°$.

with chemical potential, that is DOS $\propto |\mu|$. Thus, the tunnel conductance decreases when the graphene Fermi level crosses the Dirac point because the DOS vanishes at this point. The small but finite conductance at the Dirac point is caused by charge inhomogeneity, which results in the DOS smearing at the Dirac point and remaining non-zero[26].

The set of green lines in Fig. 2b,c traces the low bias and relatively weak resonance in the device characteristics when the chemical potential of one of the graphene layers reaches the point at which the two Dirac cones begin to overlap (Fig. 1c). These four lines satisfy the condition $\mu_{T,B} = (\Delta\varphi \pm \hbar v_F \Delta K)/2$. The intersection of these lines at $V_g = 0$ provides a good measure of the momentum mismatch $\hbar\Delta K = |e|V_b/v_F$, and therefore gives an accurate estimate of the misalignment angle, θ. For example, for the device shown in Fig. 2, we estimate that $\theta = 1.8°$. It is interesting to note the geometry of the intersection of the two Dirac cones under the conditions shown in Fig. 1c and Fig. 2: they form hyperbolic solutions. The wavevectors of the Dirac plane waves lie on three hyperbolae obtained by 120° rotations of these hyperbolic solutions (see Supplementary Section 1). The solutions remain hyperbolic for

$|\Delta\varphi| < \hbar v_F \Delta K$. This low bias resonance does not lead to NDC, but it does give rise to a significant increase in conductance, as shown in Fig. 2b.

The voltage dependence of the main resonance peak is shown as yellow lines in Fig. 2b,c. In this case, the Dirac cones are shifted by $\Delta\varphi = \pm\hbar v_F\Delta K$ so that the intersection of the cones is a straight line (that is, the wavevectors of the Dirac plane waves lie on straight lines (see Fig. 1d)). In this situation, momentum is conserved for tunnelling electrons at all energies between μ_T and μ_B, and thus gives rises to a strong peak in the current density at resonance. When the Dirac cones are displaced further beyond this resonant condition, that is for $|\Delta\varphi| > \hbar v_F\Delta K$, the curve of intersection of the two Dirac cones becomes an ellipse (Fig. 1e). In contrast to the hyperbolic and linear solutions, the elliptic solutions are bound—only wavevectors limited by these ellipses can contribute to current density. The reduction of the current once the Dirac cones are shifted off-resonance is the physical mechanism that gives rise to the NDC region beyond the resonant peak.

The main resonant peak, which would be Dirac-delta like in the absence of broadening, has a finite width because of the presence of

short-range scatterers, charge inhomogeneity in the graphene layers or orientational disorder between two graphene layers because of bubble formation[1]. Furthermore, as this mechanism of resonant tunnelling relies on momentum conservation, the position of the resonant peak and the peak-to-valley ratio are only weakly dependent on temperature. This mechanism for NDC is only possible in the graphene–graphene tunnelling system; for example, if one or both electrodes are replaced with bilayer graphene, then, because of the parabolic dispersion relation, the extended linear intersection is no longer possible. In the modelled J–V_b characteristics (Fig. 2d–f) we take into account the chirality of electrons (the momentum-dependent phase shift of the wavefunction on the two sublattices in graphene (see Supplementary Sections 1 and 2)). In the absence of strain, however, the results stay qualitatively the same.

To confirm our proposed mechanism of resonant tunnelling we performed additional measurements in which a magnetic field, $\mathbf{B}_\parallel$, was applied parallel to the graphene layers, that is, perpendicular to the tunnel current. Classically, the electron tunnelling between two 2D electrodes through a barrier of thickness d will acquire an additional in-plane momentum $ed\mathbf{l}_z \times \mathbf{B}_\parallel$ because of the action of the Lorentz force[27,28]. Depending on the orientation of the magnetic field with respect to crystallographic directions of the two graphene layers, the magnitude of the momentum transfer

$$\hbar\Delta\mathbf{K}_i^\pm = \mathbf{l}_z \times \left[\theta\hbar\mathbf{K}_i^\pm + ed\mathbf{B}_\parallel\right]$$

differs for each of the six Dirac cones at the corners of Brillouin zone.

Figure 3c,d presents the measured and calculated, respectively, tunnel conductance maps in the presence of a strong in-plane magnetic field, $\mathbf{B}_\parallel$. In Fig. 3e, the measured contour maps at zero field (Fig. 2b) and with a magnetic field ($B_\parallel = 15$ T) (Fig. 3c) are subtracted from each other. This 'difference map' reveals that the bias positions of the resonances, which correspond to various momentum-conservation conditions, are shifted significantly by the in-plane field. At the same time, the positions of the $\mu_T = 0$ and $\mu_B = 0$ resonances (which are insensitive to momentum conservation) in the dI/dV_b contour maps are almost unchanged. The fact that the in-plane magnetic field affects only the resonances where momentum-conservation processes are involved rules out possible artefacts, such as a small perpendicular component of the magnetic field.

One of the celebrated applications of devices with NDC is their use as high-frequency oscillators, which typically are constructed by connecting an external resonant circuit to the device. To this end, as a proof-of-principle we built such an oscillator by adding an inductance in series with our resonant tunnelling device when utilizing the intrinsic and parasitic capacitance (C_{tot}) as a capacitance of the LC circuit (L, inductance; C, capacitance; see Fig. 4b). When the bias and gate voltages are tuned to the NDC region, the device undergoes stable sine-wave oscillations (see Fig. 4a,c). The oscillation frequency can be tuned by varying the parameters of the external circuit (see Fig. 4b).

The operation of an NDC-based LC resonator can be understood as follows. Once excited, the LC circuit produces damped oscillations that rapidly decay to zero. This is mainly caused by the internal dissipative resistance, R, of the resonator, as well as other losses. When the tunnel transistor operates in the NDC region, its negative resistance cancels the internal lossy resistance, and thus supports continuous stable oscillations at the resonant frequency of the LC circuit. Interestingly, the shape of the J–V_b curve changes in the region of stable oscillations, as compared with the case without the LC circuit (see Fig. 4a). This is likely to be caused by the change in the asymmetric rectification of radiofrequency oscillations in the strongly nonlinear J–V_b region.

To summarize, by aligning the crystallographic orientation of the two graphene layers in a graphene/hBN/graphene heterostructure, we have demonstrated that resonant tunnelling with both energy and momentum conservation can be achieved. This results in a strong NDC that persists up to room temperature. The bias position of the resonance can be controlled by the relative orientation between the two graphene crystalline lattices and by the external magnetic field. Our tunnel diodes produce stable oscillations in the megahertz frequency range, limited mainly by the parasitic capacitance between the contact pads of our devices and the underlying Si gate. Much higher frequencies could be reached by reducing this parasitic capacitance and that of the external circuit. Even higher frequencies could also be achieved by fabricating a device in a slot antenna configuration, in which the slot acts as a resonator with the resonance frequency determined by the geometry of the slot. Moreover, our tunnel devices are free of the fundamental limitation intrinsic to conventional double-barrier resonant tunnelling devices, namely the relatively long carrier dwell time (picoseconds) in the quantum well as compared with the time to transit the barrier (femtoseconds). This suggests that, potentially, such tunnel circuits can be scaled to operate in the THz regime.

Methods

Device fabrication. The heterostructures are made by means of a standard dry-transfer procedure of mechanically exfoliated graphene and hBN layers[5,29], with the important additional step that the lattices of the top and bottom graphene flakes are aligned to within 2° of each other. We used mechanically torn graphene flakes[30] with well-defined facets and were able to distinguish between the armchair and zig-zag edges by comparing the intensity of the Raman D peak from the edges[31]. This allowed us to know the crystallographic orientation of both the top and bottom graphene, and thus achieve a high level of alignment (see Supplementary Section 3 for details). An independent proof of the crystallographic alignment between the two graphene electrodes comes from the measurements of the broadening of the Raman 2D peak for the two graphene flakes. Such broadening serves as a measure of the rotation angle between graphene and the underlying hBN[12,32], and allowed us to calculate the relative angle between the crystallographic directions for the two graphene electrodes (see Supplementary Section 3 for details). To improve its electronic quality, the bottom graphene electrode was placed on a thick layer of hBN that overlay the SiO$_2$/Si substrate, with the heavily doped Si wafer acting as a back gate[33]. The two graphene layers were independently contacted with Cr/Au metallization. We chose the thickness of the hBN tunnel barriers to be four monolayers, which allowed us to work in a comfortable range of current densities and bias voltages. The current density can be dramatically increased (4–5 orders of magnitude)[7,8] if thinner (2–3 layers) hBN or a material with a lower tunnel barrier (such as WS$_2$) is utilized[9,10,18].

References

1. Geim, A. K. & Grigorieva, I. V. Van der Waals heterostructures. *Nature* **499,** 419–425 (2013).
2. Novoselov, K. S. Nobel lecture: graphene: materials in the flatland. *Rev. Mod. Phys.* **83,** 837–849 (2011).
3. Novoselov, K. S. *et al.* Electric field effect in atomically thin carbon films. *Science* **306,** 666–669 (2004).
4. Novoselov, K. S. *et al.* Two-dimensional atomic crystals. *Proc. Natl Acad. Sci. USA* **102,** 10451–10453 (2005).
5. Ponomarenko, L. A. *et al.* Tunable metal–insulator transition in double-layer graphene heterostructures. *Nature Phys.* **7,** 958–961 (2011).
6. Gorbachev, R. V. *et al.* Strong Coulomb drag and broken symmetry in double-layer graphene. *Nature Phys.* **8,** 896–901 (2012).
7. Lee, G. H. *et al.* Electron tunneling through atomically flat and ultrathin hexagonal boron nitride. *Appl. Phys. Lett.* **99,** 243114 (2011).
8. Britnell, L. *et al.* Electron tunneling through ultrathin boron nitride crystalline barriers. *Nano Lett.* **12,** 1707–1710 (2012).
9. Britnell, L. *et al.* Field-effect tunneling transistor based on vertical graphene heterostructures. *Science* **335,** 947–950 (2012).
10. Georgiou, T. *et al.* Vertical field-effect transistor based on graphene–WS$_2$ heterostructures for flexible and transparent electronics. *Nature Nanotech.* **8,** 100–103 (2013).
11. Britnell, L. *et al.* Strong light–matter interactions in heterostructures of atomically thin films. *Science* **340,** 1311–1314 (2013).

12. Woods, C. R. *et al.* Commensurate–incommensurate transition in graphene on hexagonal boron nitride. *Nature Phys.* **10,** 451–456 (2014).
13. Xue, J. M. *et al.* Scanning tunnelling microscopy and spectroscopy of ultra-flat graphene on hexagonal boron nitride. *Nature Mater.* **10,** 282–285 (2011).
14. Yankowitz, M. *et al.* Emergence of superlattice Dirac points in graphene on hexagonal boron nitride. *Nature Phys.* **8,** 382–386 (2012).
15. Ponomarenko, L. A. *et al.* Cloning of Dirac fermions in graphene superlattices. *Nature* **497,** 594–597 (2013).
16. Dean, C. R. *et al.* Hofstadter's butterfly and the fractal quantum Hall effect in moiré superlattices. *Nature* **497,** 598–602 (2013).
17. Hunt, B. *et al.* Massive Dirac fermions and Hofstadter butterfly in a van der Waals heterostructure. *Science* **340,** 1427–1430 (2013).
18. Yang, H. *et al.* Graphene barristor, a triode device with a gate-controlled Schottky barrier. *Science* **336,** 1140–1143 (2012).
19. Haigh, S. J. *et al.* Cross-sectional imaging of individual layers and buried interfaces of graphene-based heterostructures and superlattices. *Nature Mater.* **11,** 764–767 (2012).
20. Britnell, L. *et al.* Resonant tunnelling and negative differential conductance in graphene transistors. *Nature Commun.* **4,** 1794 (2013).
21. Ponomarenko, L. A. *et al.* Field-effect control of tunneling barrier height by exploiting graphene's low density of states. *J. Appl. Phys.* **113,** 136502 (2013).
22. Feenstra, R. M., Jena, D. & Gu, G. Single-particle tunneling in doped graphene–insulator–graphene junctions. *J. Appl. Phys.* **111,** 043711 (2012).
23. de la Barrera, S. C., Gao, Q. & Feenstra, R. M. Theory of graphene–insulator–graphene tunnel junctions. *J. Vac. Sci. Technol. B* **32,** 04E101 (2014).
24. Wallbank, J. R. *Electronic Properties of Graphene Heterostructures with Hexagonal Crystals* (Springer, 2014).
25. Brey, L. Coherent tunneling and negative differential conductivity in a graphene/h-BN/graphene heterostructure. *Phys. Rev. Appl.* **2,** 014003 (2014).
26. Martin, J. *et al.* Observation of electron–hole puddles in graphene using a scanning single-electron transistor. *Nature Phys.* **4,** 144–148 (2008).
27. Hayden, R. K. *et al.* Probing the hole dispersion curves of a quantum well using resonant magnetotunneling spectroscopy. *Phys. Rev. Lett* **66,** 1749–1752 (1991).
28. Falko, V. I. & Meshkov, S. V. On resonant oscillations in current–voltage characteristics of double-barrier heterostructures. *Semicond. Sci. Technol.* **6,** 196–200 (1991).
29. Dean, C. R. *et al.* Boron nitride substrates for high-quality graphene electronics. *Nature Nanotech.* **5,** 722–726 (2010).
30. Sen, D., Novoselov, K. S., Reis, P. M. & Buehler, M. J. Tearing graphene sheets from adhesive substrates produces tapered nanoribbons. *Small* **6,** 1108–1116 (2010).
31. Neubeck, S. *et al.* Direct determination of the crystallographic orientation of graphene edges by atomic resolution imaging. *Appl. Phys. Lett.* **97,** 053110 (2010).
32. Eckmann, A. *et al.* Raman fingerprint of aligned graphene/h-BN superlattices. *Nano Lett.* **13,** 5242–5246 (2013).
33. Mayorov, A. S. *et al.* Micrometer-scale ballistic transport in encapsulated graphene at room temperature. *Nano Lett.* **11,** 2396–2399 (2011).

Author contributions

J.S.T., Y.C. and Y-J.K. fabricated devices, A.M. carried out measurements and analysed the results, J.R.W., M.T.G., T.M.F., V.I.F and L.E. provided theoretical modelling and interpretation, K.W. and T.T. provided hBN crystals, S.L.W., F.W. and C.R.W. performed atomic force microscopy and Raman measurements, R.V.G., V.E.M., S.V.M., M.J.Z., E.E.V. and O.M. helped with experiments and/or writing the paper, A.M., K.S.N. and L.E. wrote the manuscript. Sections 1 and 2 of the Supplementary Information were written by J.R.W. and V.I.F. All authors contributed to discussions.

Additional information

Supplementary information is available in the online version of the paper. Reprints and permissions information is available online at www.nature.com/reprints. Correspondence and requests for materials should be addressed to K.S.N. and L.E.

Competing financial interests

The authors declare no competing financial interests.

Twist-controlled resonant tunnelling in graphene/boron nitride/graphene heterostructures

A. Mishchenko, J. S. Tu, Y. Cao, R. V. Gorbachev, J. R. Wallbank,

M.T. Greenaway, V. E. Morozov, S. V. Morozov, M. J. Zhu,

S. L. Wong, F. Withers, C. R. Woods, Y.-J. Kim, K. Watanabe,

T. Taniguchi, E. E. Vdovin, O. Makarovsky, T. M. Fromhold,

V. I. Fal'ko, A. K. Geim, L. Eaves, K. S. Novoselov

1   Resonant tunnelling processes in graphene heterostructures

Here we describe the theoretical model for the tunnelling of Dirac electrons between two slightly misaligned graphene layers, separated by a thin layer of misaligned hBN [1–5]. Angles θ and θ_{BN}, $\theta \ll \theta_{BN}$, describe the misalignment of the top graphene layer, and the hBN layer, with respect to the bottom graphene layer. For the sake of simplicity, below we assume $|\theta| \ll |\theta_{BN}| \ll 1\,\mathrm{rad}$, and hence use $\boldsymbol{k} \cdot \boldsymbol{p}$ theory (here $\hbar = 1$). Also, we take into account that for $\theta_{BN} \gtrsim 0.04$ radians the energy scale $v_F|\sqrt{(\theta_{BN}^2 + \delta^2)}\boldsymbol{K}|$ is beyond the Fermi energy obtainable by electrostatic doping (where $\delta \sim 1.8\%$ is the graphene-hBN lattice mismatch). Then, we model a heterostructure with graphene sheets separated by a single hBN layer, so that the $\boldsymbol{k} \cdot \boldsymbol{p}$ Hamiltonian is

$$H = \begin{pmatrix} H_T & H_{\mathrm{int},T} & 0 \\ H_{\mathrm{int},T}^\dagger & H_{BN} & H_{\mathrm{int},B}^\dagger \\ 0 & H_{\mathrm{int},B} & H_B \end{pmatrix}; \quad H_{l=T/B} = v_F \begin{pmatrix} U_l/v_F & \zeta k_x - ik_y \\ \zeta k_x + ik_y & U_l/v_F \end{pmatrix}; \quad H_{BN} = \begin{pmatrix} \epsilon_N & 0 \\ 0 & \epsilon_B \end{pmatrix}.$$

Here we use a basis of the Bloch functions $(\Phi_A^T, \Phi_B^T, \Phi_N^{BN}, \Phi_B^{BN}, \Phi_A^B, \Phi_B^B)$ taken at the $K(K')$-point, $\zeta = +(-)$, from the corresponding layer. The 2×2 blocks $H_{T/B}$ describe the Dirac electrons in the top (T) or bottom (B) graphene layers, with the voltage bias $U_T - U_B = \Delta\varphi$ included. H_{BN} describes states on the nitrogen (with energy ϵ_N) and boron (with energy ϵ_B) sublattices of the hBN layer. The coupling between the graphene layers $(l = T$ or $B)$ and the hBN layer is adapted from Ref. [6] and similar theories of twisted two-layer graphene [7–12],

$$H_{int,l} = \frac{1}{3} \sum_{j=1,2,3} e^{-i\Delta\boldsymbol{K}_{T/B,j}^\zeta \cdot \boldsymbol{r}} \begin{pmatrix} \gamma_N & \gamma_B e^{-i\frac{2\pi}{3}(\zeta j - 1)} \\ \gamma_N e^{i\frac{2\pi}{3}(\zeta j - 1)} & \gamma_B \end{pmatrix}.$$

The momentum shift $\Delta\boldsymbol{K}_{l,j}^{\zeta} = \boldsymbol{K}_{l,j}^{\zeta} - \boldsymbol{K}_{BN,j}^{\zeta}$ describes the misalignment of the Brillouin zone corner of the hBN lattice, $\boldsymbol{K}_{BN,j}^{\zeta}$, from the Brillouin zone corners, $\boldsymbol{K}_{l,j}^{\zeta}$, of each of the graphene layers. The Brillouin zone corner label, j, is consistent with Fig. 1 of the main text. Also $\gamma_{N/B}$ are the hopping integral to the nitrogen sites (γ_N) or the boron sites (γ_B).

Next, we integrate out the hBN layer to obtain the effective Hamiltonian acting in the space of states in the two graphene layers,

$$H^{\text{eff}}(\epsilon) = \begin{pmatrix} H_T & 0 \\ 0 & H_B \end{pmatrix} + \delta H(\epsilon); \quad \delta H(\epsilon) \equiv \begin{pmatrix} \delta H_{TT} & \delta H_{TB} \\ \delta H_{TB}^{\dagger} & \delta H_{BB} \end{pmatrix} = \begin{pmatrix} H_{\text{int},T} \\ H_{\text{int},B} \end{pmatrix} \frac{1}{\epsilon - H_{BN}} \begin{pmatrix} H_{\text{int},T}^{\dagger} & H_{\text{int},B}^{\dagger} \end{pmatrix}.$$

The effect of the intralayer terms, δH_{TT} and δH_{BB}, consists in the formation of moiré minibands [13, 14], which modify graphene's spectra at energies $E \gtrsim v_F |\sqrt{(\theta_{BN}^2 + \delta^2)}\boldsymbol{K}|$. For $\theta_{BN} \gtrsim 2°$, this energy is higher than the energy where features in the current-voltage characteristics are formed for obtainable carrier densities in graphene, so that we only consider the effective interlayer hopping. For the same reason, we do not retain terms in $\delta H(\epsilon)$ that cause the wavevector transfer of finite hBN reciprocal lattice vector: this would scatter electrons to a high energy region of graphene's Brillouin zone that will not contribute to the tunnelling. Also, since we consider $|\epsilon| \ll |\epsilon_N|, |\epsilon_B|$, we find that

$$\delta H_{TB} = \frac{\gamma^{\text{eff}}}{3} \sum_{j=1,2,3} e^{-i\Delta\boldsymbol{K}_j^{\zeta} \cdot \boldsymbol{r}} \begin{pmatrix} 1 & e^{-i\frac{2\pi}{3}(\zeta j - 1)} \\ e^{i\frac{2\pi}{3}(\zeta j - 1)} & 1 \end{pmatrix}, \quad \text{where} \quad \gamma^{\text{eff}} = -\frac{\gamma_N^2}{3\epsilon_N} - \frac{\gamma_B^2}{3\epsilon_B}.$$

A magnetic field, $\boldsymbol{B}_{\parallel}$, applied in the plane of the device, results in an additional momentum transferred to the tunnelling electron, so that the momentum shift ($\Delta\boldsymbol{K}_j^{\zeta} = \boldsymbol{K}_{T,j}^{\zeta} - \boldsymbol{K}_{B,j}^{\zeta} \approx \theta\hat{\boldsymbol{l}}_z \times \boldsymbol{K}_j^{\zeta}$ for $\boldsymbol{B}_{\parallel} = 0$) becomes,

$$\Delta\boldsymbol{K}_j^{\zeta} = \boldsymbol{l}_z \times \left[\theta\boldsymbol{K}_j^{\zeta} + ed\boldsymbol{B}_{\parallel} \right], \tag{S.1}$$

with e the electron charge, $\boldsymbol{l}_z = (0, 0, 1)$, and d the separation between the two graphene layers. For a single-layer hBN tunnel junction we estimate $\gamma^{\text{eff}} \sim 10\,\text{meV}$ using assumptions from Ref. [6]. For a device with several hBN layers between the graphene sheets, we treat γ^{eff} as a phenomenological parameter which determines the size of the matrix elements between Dirac plane waves $|\psi_{\zeta,s_{T/B}}^{T/B}(\boldsymbol{k}_{T/B})\rangle = \frac{1}{\sqrt{2}}\left(1, \zeta s_{T/B}e^{i\zeta\phi_{\boldsymbol{k}_{T/B}}}\right)e^{i\boldsymbol{k}_{T/B}\cdot\boldsymbol{r}}$ in the two graphene layers (here $\phi_{\boldsymbol{k}} = \tan^{-1}(k_y/k_x)$ and $s_{T/B} = \pm 1$ is the band index),

$$\langle\psi_{\zeta,s_T}^T(\boldsymbol{k}_T)|\delta H_{TB}|\psi_{\zeta,s_B}^B(\boldsymbol{k}_B)\rangle = \frac{(2\pi)^2\gamma^{\text{eff}}}{3} \sum_{j=1,2,3} g\,\delta(\boldsymbol{k}_T - \boldsymbol{k}_B + \Delta\boldsymbol{K}_j^{\zeta}), \tag{S.2}$$

$$g = \frac{1}{2}\left(1 + \zeta s_B e^{-i\left(\frac{2\pi}{3}(\zeta j - 1) - \zeta\phi_{\boldsymbol{k}_B}\right)}\right)\left(1 + \zeta s_T e^{i\left(\frac{2\pi}{3}(\zeta j - 1) - \zeta\phi_{\boldsymbol{k}_T}\right)}\right).$$

Then, the Fermi golden rule for the current density, formed by the tunnelling of electron plane

2

waves between the two graphene flakes reads,

$$J = \frac{-eg_s}{(2\pi)^3} \sum_{\zeta, s_B, s_T} \int d\boldsymbol{k}_B d\boldsymbol{k}_T \frac{1}{\pi} \mathrm{Im} \frac{|\langle \psi^T_{\zeta, s_T}(\boldsymbol{k}_T)|\delta H_{TB}|\psi^B_{\zeta, s_B}(\boldsymbol{k}_B)\rangle|^2}{s_T v_F |\boldsymbol{k}_T| + \Delta\varphi - s_B v_F |\boldsymbol{k}_B| - i\gamma} (f^{\mu_B}_{s_B, \boldsymbol{k}_B} - f^{\mu_T}_{s_T, \boldsymbol{k}_T}). \qquad (S.3)$$

Here $g_s = 2$ accounts for spin degeneracy, and $f^{\mu_{T/B}}_{s_{T/B}, \boldsymbol{k}_{T/B}}$ are the occupancy numbers written using the chemical potentials $\mu_{T/B}$ on the two layers. Also, we take into account a finite broadening, γ, of electron states.

In the limit $\gamma \to 0$ the allowed tunnelling processes for electrons in each valley must simultaneously conserve both energy and momentum:

$$s_T v_F |\boldsymbol{k}_B - \Delta\boldsymbol{K}^\zeta_j| + \Delta\varphi - s_B v_F |\boldsymbol{k}_B| = 0.$$

This constraint is clearly seen in Supplementary Fig. 1, which shows the dependence of the current density on the band offset $\Delta\varphi$ for $\theta = 0.5°$ (correspondingly $v_F |\Delta\boldsymbol{K}^\zeta_j| = 0.1\,\mathrm{eV}$). The right panel of each insets shows the relative alignment of the Dirac cones on the bottom layer (grey) and the top layer (blue), for particular values of $\Delta\varphi$. The left panels show the contribution to the current density arising from states in the valley K for electrons on the bottom layer. Here the four sub-panels correspond to tunnelling between the bands: conduction to conduction, valence to conduction, valence to valence, and conduction to valence (listed clockwise from top left). The contribution of states with momentum near the valley K' can be described by rotating these images through 60°. In the absence of a magnetic field, graphene's two valleys make the same contribution to the current density, whereas in a finite $\boldsymbol{B}_\parallel$ this valley degeneracy is lifted. Depending on the value of $|\Delta\varphi| - v_F |\Delta\boldsymbol{K}^\zeta_j|$ we find that:

(i) For $|\Delta\varphi| \geq v_F |\Delta\boldsymbol{K}^\zeta_j|$ the wavevectors lie on an ellipse parametrised by $0 \leq \phi \leq 2\pi$,

$$\boldsymbol{k}_B = \begin{pmatrix} \sqrt{\frac{(\Delta\varphi/v_F)^2 - |\Delta\boldsymbol{K}^\zeta_j|^2}{4}} \sin(\phi) \\ \frac{|\Delta\varphi|}{2v_F} \cos(\phi) + \frac{|\Delta\boldsymbol{K}^\zeta_j|}{2} \end{pmatrix}, \qquad \begin{array}{l} s_B = 1, \ s_T = -1 \ \text{for} \ \Delta\varphi > 0 \\ s_B = -1, \ s_T = 1 \ \text{for} \ \Delta\varphi < 0. \end{array} \qquad (S.4)$$

This is exemplified in Supplementary Fig. 1 (a,b) which show that the dominant contribution to the current density arises from the three ellipses described by $2\pi/3$ rotations of Eq. (S.4), where the chirality factor g in Eq. S.2 modulates the tunnelling efficiency along the perimeter of each ellipse.

(ii) For $|\Delta\varphi| \leq v_F |\Delta\boldsymbol{K}^\zeta_j|$ the states lie on a hyperbola parametrised by $-\infty \leq \chi \leq \infty$,

$$\boldsymbol{k}_B = \begin{pmatrix} \sqrt{\frac{|\Delta\boldsymbol{K}^\zeta_j|^2 - (\Delta\varphi/v_F)^2}{4}} \sinh(\chi) \\ s_B \frac{\Delta\varphi}{2v_F} \cosh(\chi) + \frac{|\Delta\boldsymbol{K}^\zeta_j|}{2} \end{pmatrix}, \qquad \text{for} \ s_B = s_T = 1 \ \text{and} \ s_B = s_T = -1 \qquad (S.5)$$

This is exemplified in Supplementary Fig. 1 (e-f) where only half of each hyperbola is visible due to the chirality of the electron states in graphene.

(iii) Insets (c,d) in Supplementary Fig. 1, single out the special case $|\Delta\varphi| = v_F |\Delta\boldsymbol{K}^\zeta_j|$. Here

3
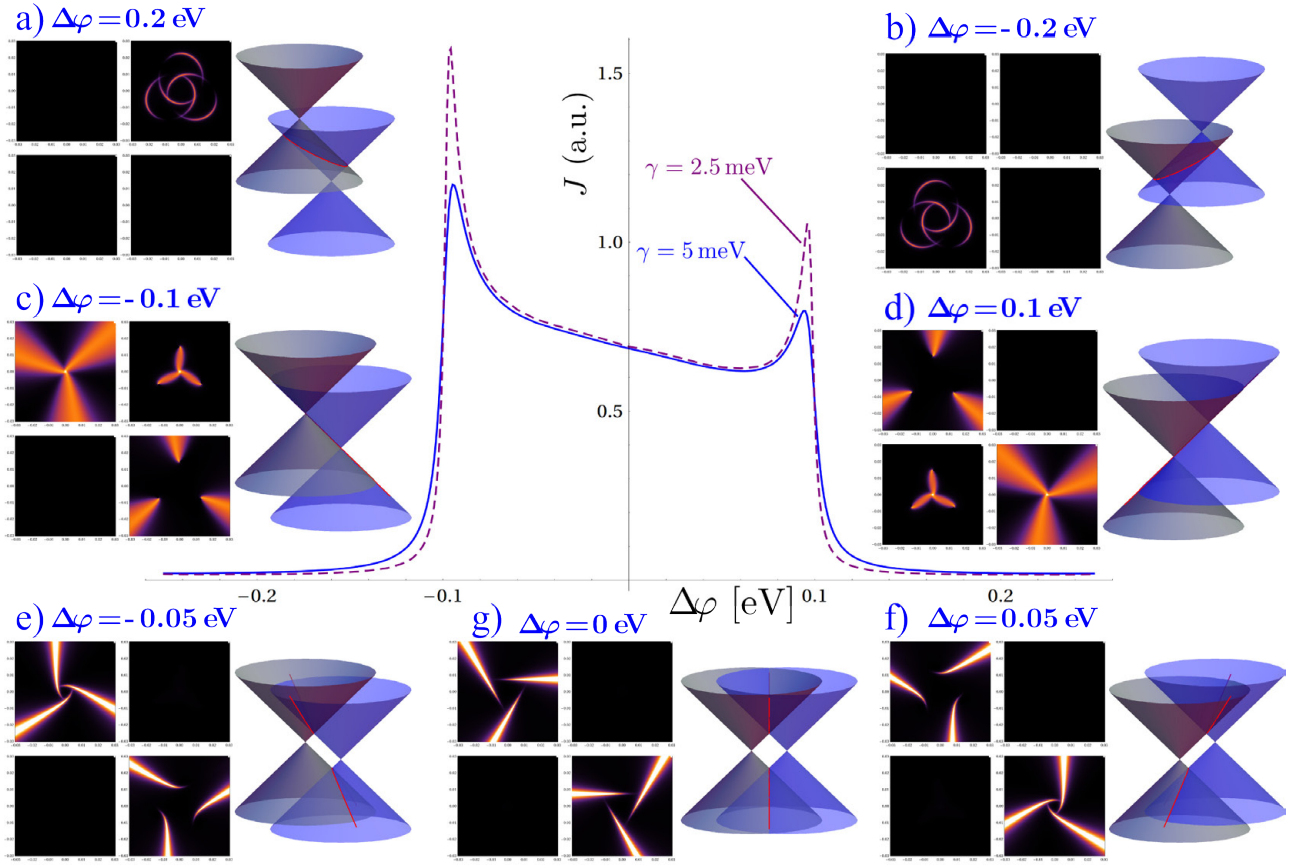
Supplementary Fig. 1: Dependence of the current density on band offset $\Delta\varphi$ for $\theta = 0.5°$, $B_\parallel = 0$, and $\mu_B = -\mu_T = 0.5\,\text{eV}$. The insets, calculated for $\gamma = 5\,\text{meV}$, show the contribution to the current density arising from states with momentum $\boldsymbol{k}_B$ in valley K of the bottom layer (see discussion in text).

the wavevectors lie on the straight lines separating elliptical (i) and hyperbolic regimes (ii). These give rise to sharp peaks in the current, the height and width of which is controlled by the broadening γ.

2 Electrostatics and the current-voltage characteristics of graphene based tunnelling transistors

The electrostatic properties of the device can be described in terms of a three-plate capacitor model. The doped n-Si (plate) is separated from the bottom graphene layer by a 290 nm-thick silicon oxide barrier and a 30 nm-thick hBN substrate layer. A hBN tunnel barrier, a few atomic layers thick, separates the two graphene electrodes. The electric field generated by charge on the gate electrode is only partly screened by the lower graphene layer, due to graphene's low density of electronic states when the chemical potential is close to the neutrality (Dirac) point. For the case of chemically undoped graphene layers which, to a good approximation, is the case in our devices, it can be shown that the bias voltage, V_b, the gate voltage, V_g, and the chemical potentials in the top (μ_T) and bottom (μ_B) graphene layers are related by the following

equation:

$$\frac{e^2 dn_T}{\epsilon_{BN}\epsilon_0} + \mu(n_T) + \mu(n_T - n_{ext}(V_g)) + eV_b = 0, \tag{S.6}$$

or equivalently, $\Delta\varphi + \mu_T - \mu_B + eV_b = 0$. Here ϵ_0 is the vacuum permittivity, d and ϵ_{BN} are the thickness and dielectric constant of hBN, respectively, and $\mu_T = \mu(n_T)$ and n_T are the Fermi energy and sheet carrier density in the top graphene electrode. The chemical potential has a square-root dependence on carrier density, n, given by $\mu(n) = \pm v_F\sqrt{\pi|n|}$. The gate-induced carrier density on the doped n-Si layer, $n_{ext}(V_g)$ is defined by the gate capacitance and gate voltage. The term $\Delta\varphi/e$ is the electrostatic voltage drop between the two graphene layers and represents the classical capacitance of the device. The Dirac cones are displaced in energy by an amount $\Delta\varphi$. The second and third terms in Eq. S.6 result from the quantum capacitance of the top and bottom graphene layers respectively [15]. By changing the bias and gate voltages, the electrochemical potentials ($\mu_{T,B}$) of the graphene layers can be adjusted interdependently.

In Supplementary Fig. 2 we have employed the electrostatic model, Eq. (S.6), to recalculate the parameters μ_B, μ_T and $\Delta\varphi$, used in Eq. (S.3), into the gate and bias voltages V_g and V_b. Supplementary Fig. 2 (a) displays the zero-magnetic-field current density J/J_0 and the differential currents $\frac{dI}{dV_b}R_0$ and $\frac{dI^2}{dV_b^2}R_1^2$, normalised to their peak values J_0, R_0^{-1}, and $R_1^{-1/2}$ obtained at the values of V_b and V_g marked by a white crosses in the figure. Maxima in J/J_0 and corresponding features in $\frac{dI}{dV_b}R_0$ and $\frac{dI^2}{dV_b^2}R_1^2$, occur along such lines on the V_b-V_g plane that $|\Delta\varphi| = v_F|\Delta\boldsymbol{K}_j^\zeta|$, and are visible in the main panels of Supplementary Fig. 2(a). Features corresponding to the characteristic lines $\mu_{T/B} = 0$ and $\mu_{T/B} = (\Delta\varphi \pm v_F|\Delta\boldsymbol{K}_j^\zeta|)/2$ (discussed in main text) are more clearly visible in the insets in Supplementary Fig. 2.

Supplementary figures 2 (b,c) show the normalised current density for two orientations of the in-plane magnetic field, $B_\parallel = 15\,\mathrm{T}$. Here the length of the in-plane wavevector transferred upon tunnelling ($|\Delta\boldsymbol{K}_j^\zeta|$, Eq. (S.1)) may be different for each of the six Brillouin zone corners $\boldsymbol{K}_j^\zeta$. Hence the features associated with the characteristic lines $|\Delta\varphi| = v_F|\Delta\boldsymbol{K}_j^\zeta|$ and $\mu_l = (\Delta\varphi \pm v_F|\Delta\boldsymbol{K}_j^\zeta|)/2$ (which depend on $|\Delta\boldsymbol{K}_j^\zeta|$) are split into multiple features in Supplementary Fig. 2(b,c). Note that the higher value of broadening, $\gamma = 40\,\mathrm{meV}$, in Supplementary Fig. 3 (d,f) of the main text, as compared to $\gamma = 5\,\mathrm{meV}$ in Supplementary Fig. 2, obscures the above mentioned peak splitting so that the effect of the magnetic field is more subtle. This is illustrated in Supplementary Fig. 3, which displays the normalised current, for cuts in the V_g-V_b plane at constant gate voltage, for both $\gamma = 5\,\mathrm{meV}$ (panels a-c) and $\gamma = 40\,\mathrm{meV}$ (panels d-f).

3 Crystallographic alignment of graphene layers

Devices were fabricated using the standard dry-transfer procedure [16], with one critical step added: during transfer the crystallographic orientations of the two graphene flakes were aligned to within 2°, see 4e. To this end, for the device fabrication we selected mechanically exfoli-

5
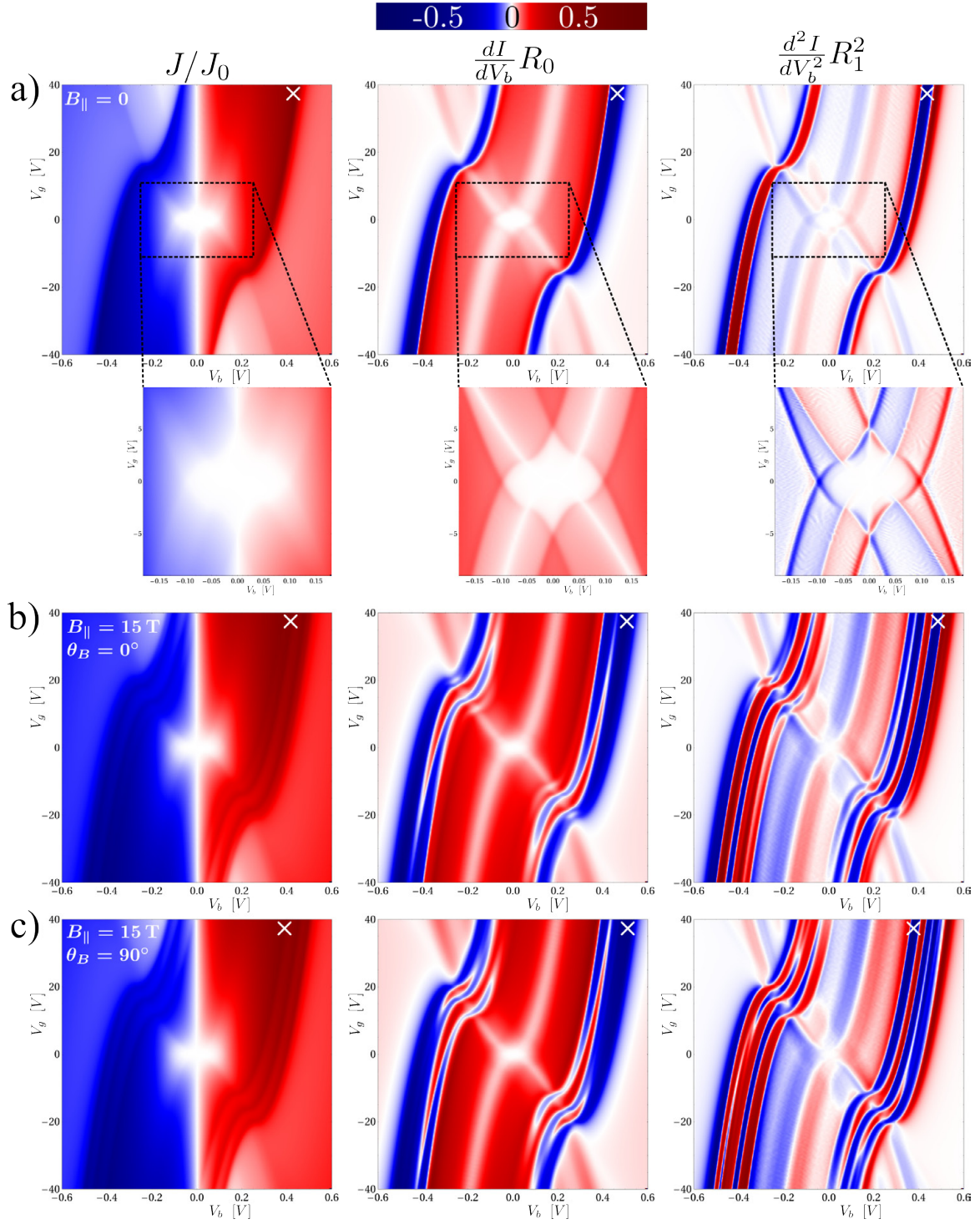
Supplementary Fig. 2: a) The current density J/J_0 and the differential currents $\frac{dI}{dV_b}R_0$ and $\frac{dI^2}{dV_b^2}R_1^2$, normalised to their peak values J_0, R_0^{-1}, and $R_1^{-1/2}$ obtained at the values of V_b and V_g marked by a white crosses. Insets show the enlargement of the regions marked with dashed lines. b-c) The same as (a) but including 15 T in-plane magnetic fields oriented either perpendicular ($\theta_B = 0°$) or parallel ($\theta_B = 90°$) to the carbon-carbon bonds in the bottom graphene layer (zig-zag or armchair directions).

6
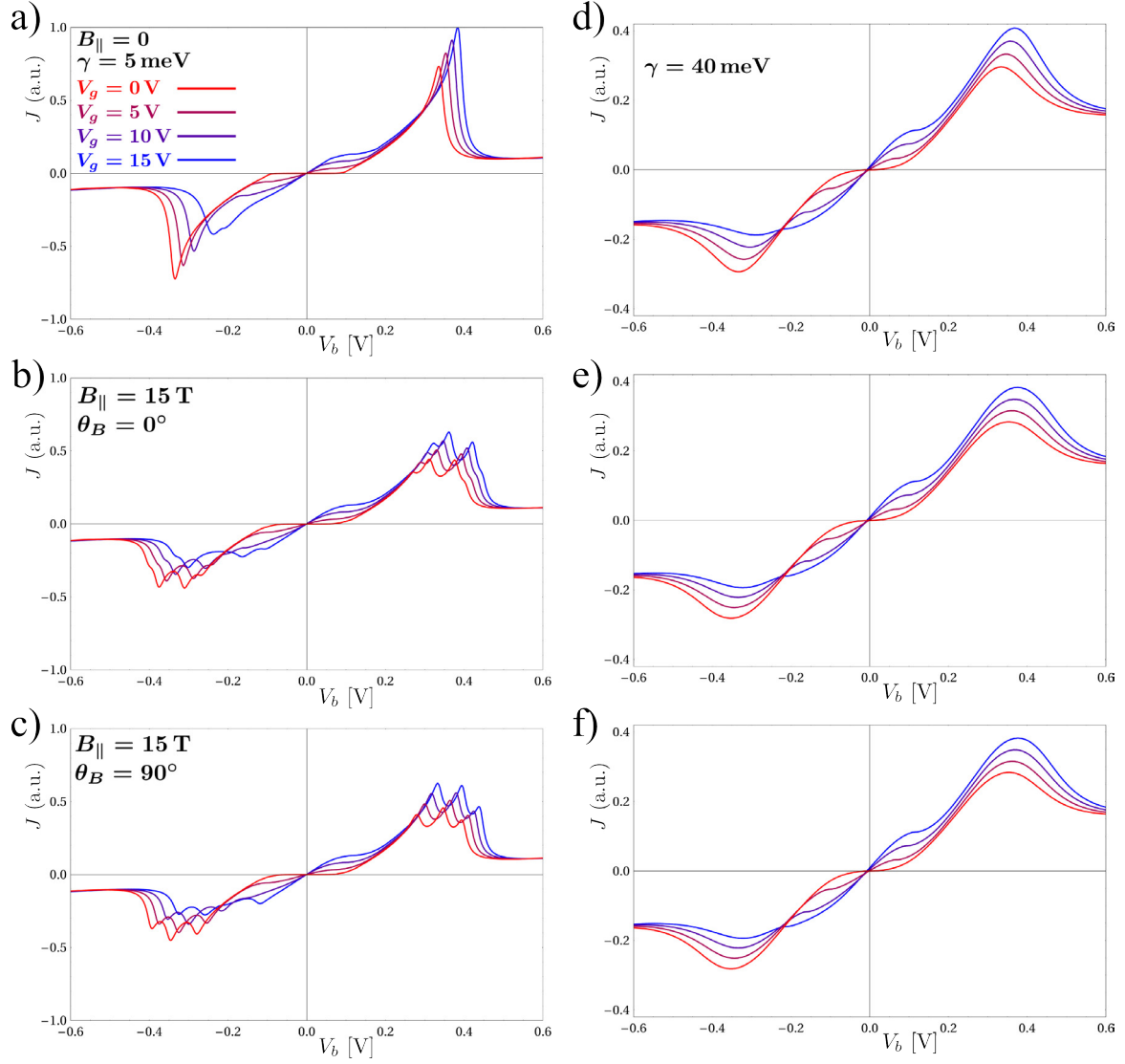
Supplementary Fig. 3: The dependence of the current density (normalised to its highest obtained value in (a)) for various gate voltages. Results are shown for the broadening $\gamma = 5\,\text{meV}$ and $B_{\parallel} = 0$ as well as for two orientations of a $15\,\text{T}$ in-plane magnetic field (b,c). Panels (d-f) show the same as (a-c) but for $\gamma = 40\,\text{meV}$.

ated graphene flakes with edges oriented along crystallographic directions (so the facets of the flakes comprise angles of multiples of 30°). Typically we use narrow ribbons (few micrometre across) as the top and bottom graphene electrodes, so they form a junction of several square micrometres in area at the place of their crossing, when oriented at 90° to each other.

We employ Raman spectroscopy in order to distinguish between zig-zag and armchair edges and thus determine the crystallographic orientation of flakes with well-defined facets. It has been shown previously [17] that the zig-zag edge of graphene should not produce any D peak, in contrast to armchair edge. In reality, because the graphene edges are not perfect (even though predominantly oriented) the typical ratio for the amplitude of the D peak from armchair and zig-zag edges is around 1.5, Supplementary Fig. 4c,d [18].

Raman spectroscopy was performed at room temperature in the backscattering geometry using a Renishaw inVia Raman microscope. A grating with 2400 lines mm^{-1} was used, providing a spectral resolution of ± 1 cm^{-1}. An excitation laser source of 514 nm with power less than 0.7 mW was used in the measurements, using a 100x objective. The excitation source is linearly polarised in the horizontal direction of the sample plane. No peak evolution due to heating or beam damage were observed during each individual scan. Peak intensity maps were obtained from fits of the graphene-associated Raman D peak with baseline corrections accounted for.

Supplementary Fig. 4a,b presents the spatial map of the Raman D peak amplitude for the top and bottom flakes. By comparing the amplitude of the D peak from the long edges of the top and bottom graphene electrodes (4d) we confirm that they most probably have different chirality (zig-zag for the top graphene electrode and armchair for the bottom), which confirms that the two electrodes are crystallographically aligned.

Moreover, it has been demonstrated previously that due to the reconstruction of graphene lattice, the Raman spectrum of graphene on hBN changes [19] if the misorientation angle between the two crystals is less than 5°. In particular, the 2D peak becomes significantly broadened. This gives one a tool to determine the relative orientation of graphene with respect to hBN.

By comparing the broadening of the 2D peak of the top and bottom graphene electrodes (in case they both rest on the same monocrystalline flake of hBN) one can conclude on the relative orientation between the two electrodes. This technique, however, is limited to the cases when crystallographic orientation of the graphene flakes is within 5° with respect to that of hBN.

Supplementary Fig. 5 presents measurements of the broadening of the 2D peak for the top and bottom graphene for the device presented in Supplementary Fig. 4. Measurements suggest that the top and bottom graphene crystals are aligned to the crystallographic orientation of the underlying substrate hBN by $\pm 2°$ and $\pm 3°$ degrees respectively. This means that the graphene layers are misoriented with respect to each other either by 1 degree (if the sign of misorientation to hBN is the same) or by 5 degrees (if the misorination to hBN is of the opposite signs). The position of the resonances in the tunnelling current suggest that indeed, the flakes are misoriented by 1°.
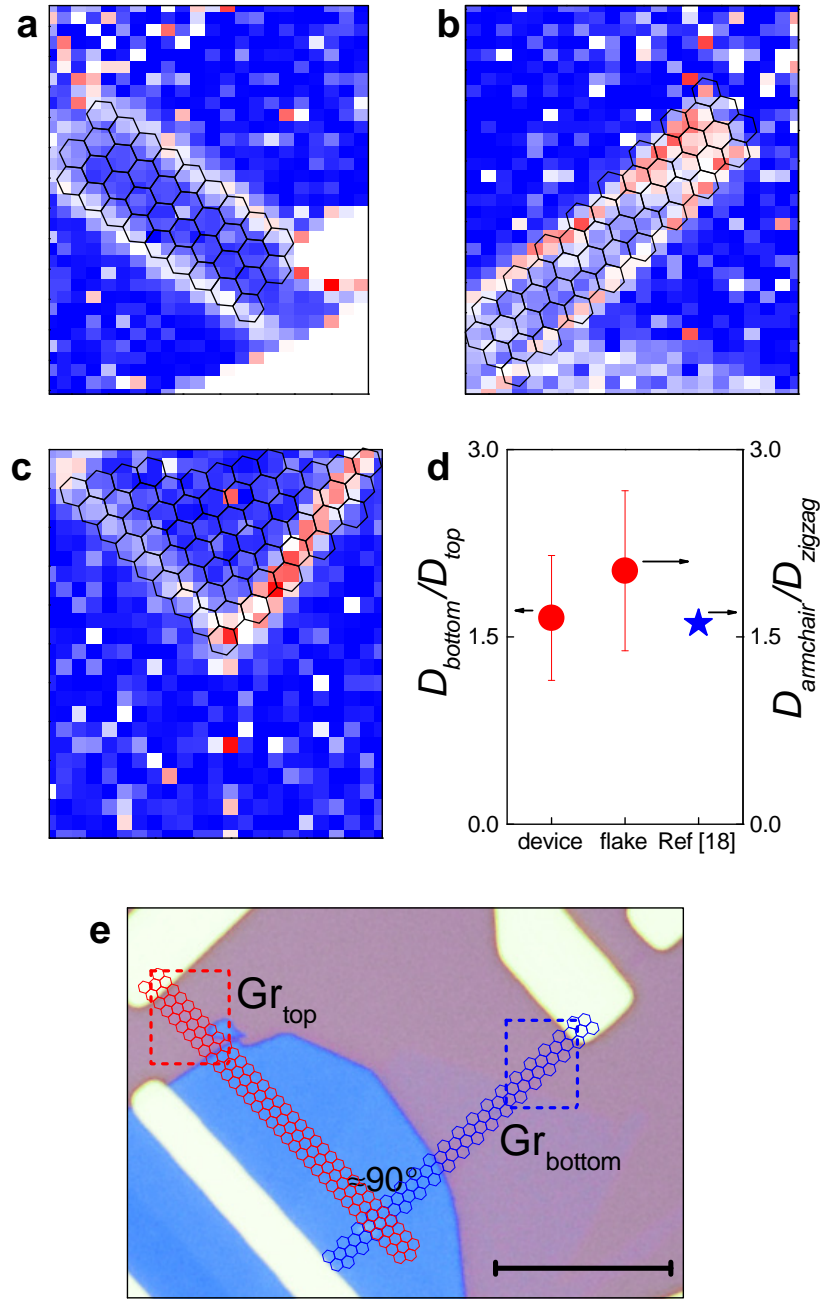
Supplementary Fig. 4: Crystallographic alignment of the two graphene layers in the resonant tunnelling device (shown in panel (e)). Panels (a-c) show Raman D peak intensity maps - top (a) and bottom (b) graphene layers for device, and mechanically exfoliated graphene flake (c) with 90° angle between edges. Laser is linearly polarized along horizontal axis. Panel (d) is the D peak intensity ratio between armchar to zigzag edges. Panel (e) is the optical micrograph of the studied device, scale bar 10 μm. Red and blue rectangles outline regions mapped on panels (a) and (b), respectively.

9
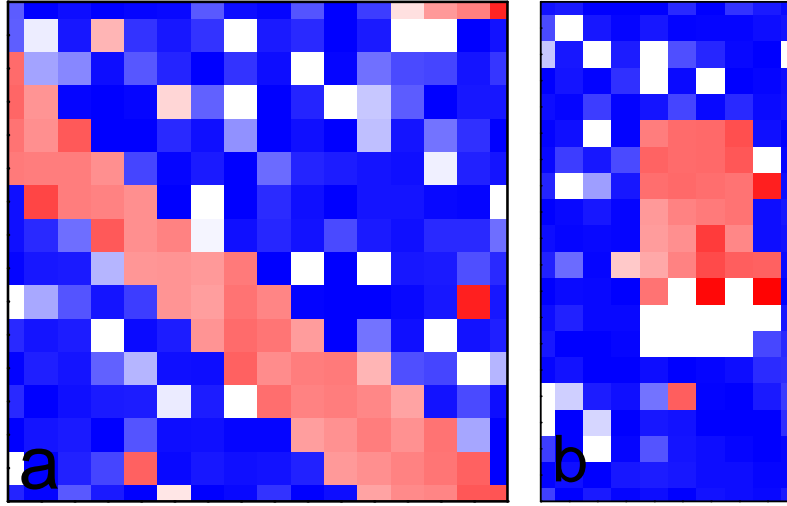
Supplementary Fig. 5: Crystallographic alignment of the two graphene layers in the resonant tunnelling device (device shown in 4e). Panels show Raman 2D peak full width at half maximum maps: top (a) and bottom (b) graphene layers for device. Scale: blue to white to red, 0 to 15 to 30 cm^{-1}. Pixel size is 0.5 μm.

4 Results obtained for other devices

We fabricated several aligned devices. The data for one of the devices is presented in the main text. Supplementary Fig. 6 shows $J - V_b$ characteristics as well as contour plots of dI/dV_b and d^2I/dV_b^2 for two more aligned devices.

5 Room Temperature Operation

In Supplementary Fig. 7 we demonstrate the room temperature operation of the device presented in the main text.

6 Comparison with resonant tunnelling in conventional resonant tunnelling devices

Previously, it has been demonstrated that graphene/hBN/graphene devices should not exhibit instabilities which would result in intrinsic oscillations [20]. In conventional double barrier resonant tunnelling devices (DBRTDs), the build-up of charge in the quantum well leads to a delay of the current with respect to the voltage which can be represented in terms of an inductance in the equivalent circuit of the device [21–23]. This effective inductance, which is an important feature in the operation of DBRTD oscillators, is absent in our single barrier devices [20].

10
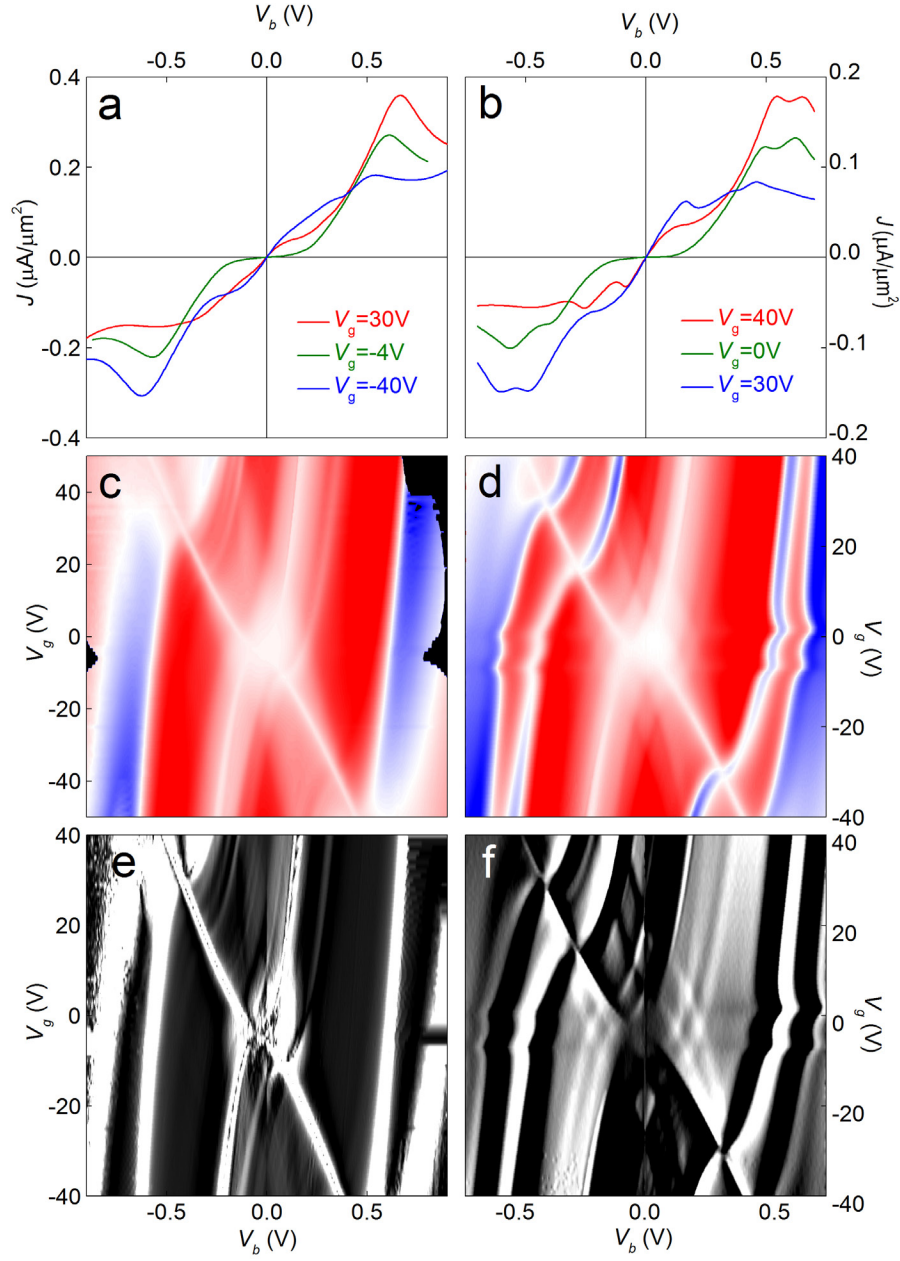
Supplementary Fig. 6: Tunnelling characteristics of two additional devices with different misalignment angles. $T = 2\,\mathrm{K}$. Left panels - device with $0.9°$ misalignment angle, right panels - device with two misalignment angles: $0.6°$ and $1.1°$, possibly due to the presence of a large bubble in the active area of device. a) and b) $J - V_b$ characteristics, c) and d) dI/dV_b contour plots, e) and f) $|d^2I/dV_b^2|$ contour plots. Device area: $120\,\mu\mathrm{m}^2$ for a, c, e and $100\,\mu\mathrm{m}^2$ for b, d, f.
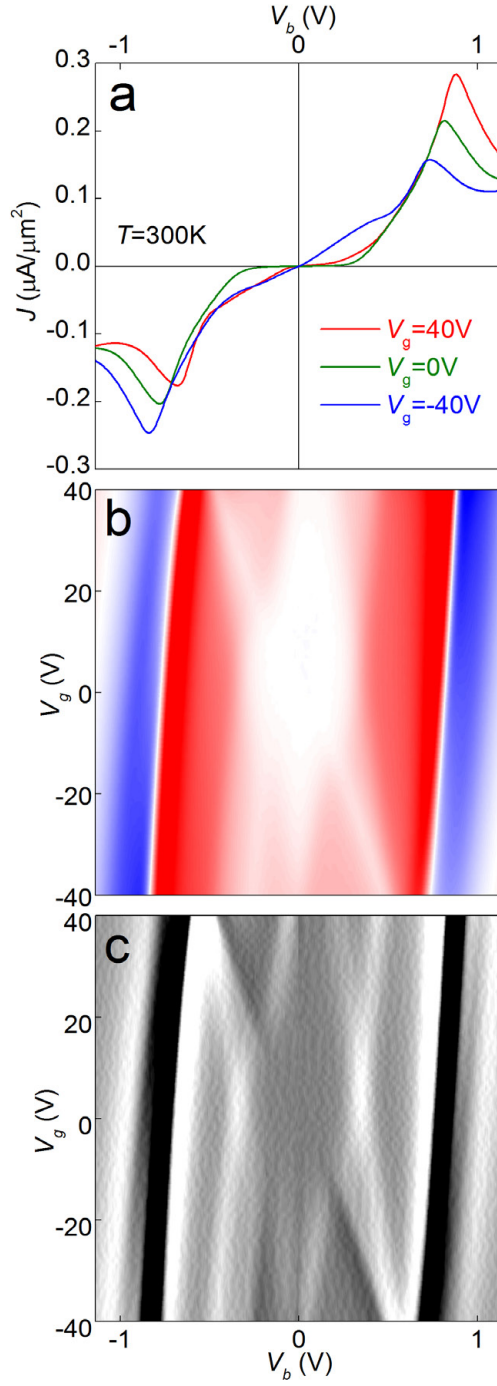
Supplementary Fig. 7: Tunnelling characteristics of the device presented in main text, measured at 300 K. a) $J - V_b$ characteristics, b) dI/dV_b contour plot, c) $|d^2I/dV_b^2|$ contour plot.

References

[1] Feenstra, R. M., Jena, D. and Gu, G. Single-particle tunneling in doped graphene-insulator-graphene junctions. *J. Appl. Phys.* **111**, 043711 (2012).

[2] Vasko, F. T. Resonant and nondissipative tunneling in independently contacted graphene structures. *Phys. Rev. B* **87**, 075424 (2013).

[3] Barrera, S. C., Gao, Q. and Feenstra, R. M. Theory of graphene-insulator-graphene tunnel junctions. *J. Vac. Sci. Technol. B* **32**, 04E101 (2014).

[4] Wallbank, J. R. *Electronic Properties of Graphene Heterostructures with Hexagonal Crystals* (Springer PhD Thesis Series, Springer, 2014); ISBN 978-3-319-07721-5.

[5] Brey, L. Coherent tunneling and negative differential conductivity in graphene-hBN-graphene heterostructure. *Phys. Rev. Applied* **2**, 014003 (2014).

[6] Kindermann, M., Uchoa, B. and Miller, D. L. Zero-energy modes and gate-tunable gap in graphene on hexagonal boron nitride. *Phys. Rev. B* **86**, 115415 (2012).

[7] Lopes dos Santos, J. M. B., Peres, N. M. R., and Castro Neto, A. H. Graphene Bilayer with a Twist: Electronic Structure. *Phys. Rev. Lett.* **99**, 256802 (2007).

[8] Bistritzer, R. and MacDonald, A. H. Transport between twisted graphene layers. *Phys. Rev. B* **81**, 245412 (2010).

[9] Kindermann, M. and First, P. N. Local sublattice-symmetry breaking in rotationally faulted multilayer graphene. *Phys. Rev. B* **83**, 045425 (2011).

[10] Bistritzer, R. and MacDonald, A. H. Moiré butterflies in twisted bilayer graphene. *Phys. Rev. B* **84**, 035440 (2011).

[11] Mele, E. J. Band symmetries and singularities in twisted multilayer graphene. *Phys. Rev. B* **84**, 235439 (2011).

[12] Lopes dos Santos, J. M. B., Peres, N. M. R. and Castro Neto, A. H. Continuum model of the twisted graphene bilayer. *Phys. Rev. B* **86**, 155449 (2012).

[13] Ortix, C., Yang, L. and van den Brink, J. Graphene on incommensurate substrates: Trigonal warping and emerging Dirac cone replicas with halved group velocity. *Phys. Rev. B* **86**, 081405 (2012).

[14] Wallbank, J. R., Patel, A. A., Mucha-Kruczynski, M., Geim, A. K., and Fal'ko, V.I. Generic miniband structure of graphene on a hexagonal substrate. *Phys. Rev. B* **87**, 245408 (2013).

[15] Yu, G. L., Jalil, R., Belle, B., Mayorov, A. S., Blake, P., Schedin, F., Morozov, S. V., Ponomarenko, L. A., Chiappini, F., Wiedmann, S., Zeitler, U., Katsnelson, M. I., Geim, A. K., Novoselova, K. S., Eliasa, D. C. Interaction phenomena in graphene seen through quantum capacitance. *Proc. Natl. Acad. Sci. U.S.A.* **110**, 3282, (2013).

[16] Ponomarenko, L. A., Geim, A. K., Zhukov, A. A., Jalil, R., Morozov, S. V., Novoselov, K. S., Grigorieva, I. V., Hill, E. H., Cheianov, V. V., Falko, V. I., Watanabe, K., Taniguchi, T., Gorbachev, R. V. Tunable metal-insulator transition in double-layer graphene heterostructures. *Nat. Phys.* **7**, 958 (2011).

[17] Casiraghi, C., Hartschuh, A., Qian, H., Piscanec, S., Georgi, C., Fasoli, A., Novoselov, K. S., Basko, D. M., Ferrari, A. C. Raman Spectroscopy of Graphene Edges. *Nano Letters* **9**, 1433 (2009).

[18] Neubeck, S., You, Y. M., Ni, H., Blake, P., Shen, Z. X., Geim, A. K., Novoselov, K. S. Direct determination of the crystallographic orientation of graphene edgesby atomic resolution imaging. *Apl. Phys. Lett.* **97**, 053110 (2010).

[19] Eckmann, A., Park, J. S., Yang, H. F., Elias, D., Mayorov, A. S., Yu, G. L., Jalil, R., Novoselov, K. S., Gorbachev, R. V., Lazzeri, M., Geim, A. K., Casiraghi, C. Raman Fingerprint of Aligned Graphene/h-BN Superlattices. *Nano Letters* **13**, 5242 (2013).

[20] Ryzhii, V., Satou, A., Otsuji, T., Ryzhii, M., Mitin, V., Shur, M. S. Dynamic effects in double graphene-layer structures with inter-layer resonant-tunnelling negative conductivity. *J. Phys. D: Appl. Phys.* **46**, 315107 (2013).

[21] Frensley, W. R. Quantum transport calculation of the smallsignal response of a resonant tunneling diode. *Apl. Phys. Lett.* **51**, 448 (1987).

[22] Mains, R. K., Haddad, G. I. Timedependent modeling of resonanttunneling diodes from direct solution of the Schrdinger equation. *J. Appl. Phys.* **64**, 3564 (1988).

[23] Mizuta, H., Tanoue, T. *The physics and applications of resonant tunnelling diodes*, 134-140 (Cambridge University Press, 1995).